Coastal Engineering 183 (2023) 104337

Contents lists available at ScienceDirect

Coastal Engineering

journal homepage: www.elsevier.com/locate/coastaleng

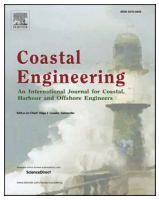

Simultaneous mapping of nearshore bathymetry and waves based on physics-informed deep learning

Qin Chen [a,*], Nan Wang [b,**], Zhao Chen [c,b]

[a] Department of Civil and Environmental Engineering, Department of Marine and Environmental Sciences, Northeastern University, Boston, MA, 02115, USA
[b] Department of Civil and Environmental Engineering, Northeastern University, Boston, MA, 02115, USA
[c] Department of Bridge Engineering, Southeast University, 2 Southeast University Road, Nanjing, 211189, Jiangsu, China

ARTICLE INFO

Keywords:
Physics-informed neural networks
Depth inversion
Wave field reconstruction
Nearshore bathymetry mapping
Scientific machine learning

ABSTRACT

This paper uses physics-informed neural networks (PINNs) to simultaneously determine nearshore water depths and wave height fields based on remote sensing of the ocean surface with limited or sparse measurements. Two methods that integrate the knowledge of water wave mechanics and fully connected neural networks are introduced. The first method utilizes observed wave celerity fields and scarce measurements of wave height as training data. The model performance was examined with linear waves over an alongshore varying barred beach and nonlinear waves over an alongshore uniform barred beach. The second method uses scarce wave height and water depth measurements as training points, and the model performance was investigated with water waves over a circular shoal and the alongshore varying barred beach. One advantage of applying PINNs to solve bathymetry inversion problems is that wave height and bathymetry can be simultaneously estimated by PINN models. Thus, the impact of wave amplitude dispersion on depth inversion in nonlinear wave systems can be considered without measuring the entire wave height field. Overall, this study demonstrates the potential of the inverse PINN model as a promising tool for estimating nearshore bathymetry and reconstructing wave fields using observations from different remote sensing platforms.

1. Introduction

Due to increasing coastal utilization and sea level rise, accurate information about nearshore bathymetry is essential for designing and operating many coastal projects, such as flood protection and coastal zone management. To better forecast nearshore wave characteristics, it is critical to use precise nearshore bathymetric data as an input to hydrodynamic models, because the accuracy of bathymetry is considered one of the most severe limitations in predicting nearshore waves and currents (e.g., Van Dongeren et al., 2008; Salim and Wilson, 2021). In general, it is costly to collect nearshore bathymetric data using in-situ methods, such as vessel-based (Dugan et al., 2001; Ruggiero et al., 2005) and bottom contact (Birkemeier and Mason, 1984) surveying techniques. Also, conventional surveying methods become impractical due to the hazardous surf zone conditions during storms. Even when in-situ measurements are available, the spatial undersampling may not resolve complex bathymetric features, and temporal undersampling may also poorly capture beach changes in a highly dynamic environment. Therefore, it would be desirable to monitor the nearshore regions (e.g., wave celerity and wave height) with the help of remote sensing techniques, which have a broader spatial and temporal coverage than the traditional in-situ surveying methods (e.g., Gallego et al., 2011; Wilson et al., 2014).

Previous technologies for estimating nearshore bathymetry using remote sensing methods include LiDAR (e.g., Wilson and Berezhnoy, 2018; Blenkinsopp et al., 2012), radar (Haller et al., 2014), infrared (Dugan et al., 1996) etc. In the past several decades, many studies have focused on solving bathymetric inversion problems using observed surface wave properties (e.g., water surface elevation and wave celerity) and simple physical models. For example, cBathy is a popular bathymetric inversion algorithm that uses the linear wave dispersion relationship to estimate nearshore bathymetry with wave celerity obtained from remote sensing techniques and a Kalman-filtered update framework (Holman et al., 2013). The algorithm was found to deteriorate

* Corresponding author.
** Corresponding author.
E-mail addresses: q.chen@northeastern.edu (Q. Chen), wang.nan@northeastern.edu (N. Wang), zhaochenseu@outlook.com, chen.zhao1@northeastern.edu (Z. Chen).

https://doi.org/10.1016/j.coastaleng.2023.104337
Received 22 November 2022; Received in revised form 9 April 2023; Accepted 13 May 2023
Available online 14 May 2023

during storms when waves transition from non-breaking to breaking in the surf zone (Honegger et al., 2019). To improve the simulation accuracy nearshore, a number of studies used nonlinear wave dispersion relationships (Grilli, 1998; Catálan and Haller, 2008; Ge et al., 2020; Martins et al., 2023) and wave breaking dissipation proxies (Aarninkhof et al., 2005) to infer bathymetric changes. For example, Yoo et al. (2011) inverted water depth in the surf zone with the inclusion of wave nonlinearity using wave celerity obtained from remotely captured videos. They found good agreement between the predicted and measured water depths for depths ranging from 0.1 m to 3 m. Moreover, Kennedy et al. (2000) reconstructed bathymetry using two snapshots of water surface elevations and velocities based on the Boussinesq wave model (Chen et al., 1999). They employed the phase speed difference in the computed and measured data as the basis for updating bathymetry at each iteration.

Another popular bathymetry inversion technique is data assimilation, which combines observational data and dynamical systems to generate a state estimation while accounting for uncertainty in the observations and model dynamics (Lewis et al., 2006; Birrien et al., 2013; Wilson and Berezhnoy, 2018). Data assimilation tries to minimize a cost function based on the difference between observations and simulations with an initial estimate of the unknown parameters and uncertainties to regularize the solution (Salim and Wilson, 2021). During the past several decades, significant progress has been made in utilizing data assimilation to estimate bathymetry in shallow water areas. For example, Van Dongeren et al. (2008) estimated bathymetry variations with good accuracy using the Kalman filtering method based on remote sensing data (i.e., wave roller dissipation, intertidal shoreline, and wave celerity). Furthermore, Wilson et al. (2014) estimated bathymetry as an uncertain parameter in a data assimilation system with the ensemble Kalman filter based on time-dependent remote sensing observations (i.e., wave celerity, alongshore current, and shoreline observations). The results show that nearshore bathymetry can be estimated with good accuracy, and nearshore hydrodynamic forecasts can be improved by assimilating remotely sensed data. Salim and Wilson (2021) tested the accuracy of the depth inversion model by assimilating in-situ wave height and alongshore current observations at a barred beach in Duck, NC, USA. They found that the results had an average root-mean-square error of 0.46 m when assimilating both the observed parameters simultaneously, which increased to 0.69 m when assimilating only alongshore current observations but decreased to 0.44 m when assimilating only wave height observations.

Recently, the development of machine learning (ML) methods, computer hardware, and remote sensing technologies has created new opportunities for using soft computing-based models to estimate nearshore bathymetry (e.g., Eldesokey et al., 2019; Dhamo et al., 2019). Unlike the data assimilation method, soft-computing models do not require simulations from deterministic forward numerical models or knowledge about the uncertainty of observations and the uncertainty of the numerical model. Using the data assimilation method to solve the inverse problem can be computationally expensive, since it may require thousands or millions of forward model simulations for evaluating estimators and characterizing posterior distributions of parameters (Willard et al., 2020). Thus, applying ML to obtain the solution to inverse problems would be desirable, because it can execute faster than numerical models and simulate high-dimensional scenarios with a large amount of data. For instance, Collins et al. (2020) used deep convolutional neural networks (DCNNs) to estimate nearshore bathymetry based on time-averaged and snapshot synthetic imagery. They found that DCNNs show robustness in depth estimation with wave heights up to 2.5 m, unlike the above-mentioned physics-based depth inversion methods that show larger errors when wave heights become higher. Additionally, they stated that ML techniques bring opportunities for more accurate predictions of nearshore bathymetry without linear simplification of input data or physical models. Other examples of applying data-driven models to solve inverse problems include photonics (Pilozzi et al., 2018), seismic processing (Vamaraju and Sen, 2019), medical imaging (Lunz et al., 2018), and remote sensing of surface properties (Dawson et al., 1992), among others.

Another ML-based approach for solving inverse problems is physics-informed neural networks (PINNs), which embed physics with the soft-computing learning algorithm. Unlike traditional ML methods, PINNs can be generalized to predict scenarios that are unseen in the training datasets. Furthermore, PINNs require a smaller amount of training datasets than traditional ML methods, which is very useful in coastal engineering applications because field measurements are often limited in reality. Using PINNs to solve inverse problems has been the focus of many recent studies. For example, Raissi et al. (2019) predicted the lift and drag forces of a system based on sparse data of the velocity field with a physics-guided loss function. Furthermore, Kahana et al. (2020) applied a neural network with a physically informed loss component to identify the location of an underwater obstacle. The results show that the model can generalize well and produce promising results.

In this study, inverse models were developed to estimate nearshore bathymetry based on remote sensing data (i.e., wave number and significant wave height) with PINNs. Meanwhile, the feasibility of reconstructing both the concurrent bathymetry and wave height field in shallow water with scarce wave and depth measurements was investigated. Nearshore wave processes, including wave shoaling, refraction, and depth-induced breaking, were considered in the model. To the best of our knowledge, this is the first time that PINNs are applied to solve the inverse problem of predicting bathymetry in shallow waters. The rest of the paper is organized as follows. Section 2 provides essential information on the governing equations. Details of the model setup for PINNs are also introduced in this section. Section 3 examines the performance of PINNs in simultaneously mapping bathymetry and reconstructing nearshore wave fields. Section 4 discusses the advantage of using PINNs for solving depth inversion problems and the influences of the location of training data on the performance of PINNs as well as using transfer learning to improve the model efficiency for changing conditions. Finally, Section 5 concludes the paper with remarks on this study.

2. Methodology

Because remote sensing is capable of observing a broad spatiotemporal range of geophysical parameters, it can be applied as a valuable tool for monitoring the nearshore, such as video cameras, radar, infrared, and LiDAR (Wilson et al., 2014). In this study, we take a simplified approach by only using synthetic model data as opposed to actual remotely-sensed data to determine the model performance of PINNs. Therefore, the digital image processing of remote sensing data is not covered in this study. Moreover, it is assumed that the free surface parameters derived from remote sensing data are sufficiently accurate in this work.

This study determines the water depth and wave fields with two methods.

- Method A: We assumed that the surface wave celerity (or wave number) and limited wave height measurements are available from various remote sensing platforms. Then, the concurrent bathymetry and wave height fields were inferred by the inverse PINNs developed with wave number and scarce wave height measurements as the training data. The performance of this method was investigated by solving the depth inversion problem over an alongshore varying barred beach with the simulation data from XBeach (Roelvink et al., 2009). Also, we examined the effects of amplitude dispersion (i.e., nonlinear dispersion relation) on depth inversion and wave prediction using monochromatic waves over an alongshore uniform barred beach as an example.
- Method B: Notice that when the wave number data are unavailable, PINN models could still be utilized to simultaneously map the bathymetry and reconstruct wave fields if wave heights and water

depths at limited locations are partially known. Our second method uses the scarce measurements of wave height and water depth to train the PINNs for solving the depth inversion problems without any observations of wave celerity or wave number. The model performance was examined by estimating the bathymetry and reconstructing wave fields over a circular shoal with the laboratory experiment data from Chawla et al. (1996). Moreover, this method was investigated by solving the depth inversion problem over the alongshore varying barred beach under field conditions in Duck, NC, USA. Although this test case is the same as the one used for examining Method A, it is worth mentioning that the training data and network structures are different from those in Method A.

2.1. Energy balance equation for wave propagation in the nearshore

In this study, we developed PINN models to solve depth inversion problems and reconstruct wave fields in the nearshore area. This study focused on stationary wave fields without wind forcing and ambient currents. Wave shoaling, refraction, and depth-limited breaking were considered in this model. The governing equations encoded into the fully connected neural networks include the wave energy balance equation and dispersion relation. The effect of amplitude dispersion (i.e., nonlinear dispersion relation) on depth inversion and wave field reconstruction was also investigated. For water waves, the energy balance equation is given by

$$\frac{\partial ec_{gx}}{\partial x}+\frac{\partial ec_{gy}}{\partial y}+\frac{\partial ec_{g\theta}}{\partial \theta}+d_w=0 \tag{1}$$

where e is the wave energy density in each directional bin, c_g is the group velocity, $\boldsymbol{\theta}$ represents the angle of incidence with respect to the x-axis, and d_w is the dissipation of energy density caused by wave breaking. c_{gx}, c_{gy}, and $c_{g\theta}$ are formulated as

$$c_{gx}(x,y,\theta)=c_g\cos\theta \tag{2}$$

$$c_{gy}(x,y,\theta)=c_g\sin\theta \tag{3}$$

$$c_{g\theta}(x,y,\theta)=\frac{\omega}{\sinh 2kh}\left(\frac{\partial h}{\partial x}\sin\theta-\frac{\partial h}{\partial y}\cos\theta\right) \tag{4}$$

representing the wave propagation speeds in x, y, and directional space, respectively. h is the local water depth, k represents the wave number, and ω is the angular frequency. The Janssen and Battjes (2007) formulation for wave breaking was applied in this study. The total wave dissipation was distributed proportionally over the wave directions using the following formulation

$$d_w(x,y,\theta)=\frac{e(x,y,\theta)}{E(x,y)}\overline{D}_w(x,y) \tag{5}$$

where $\overline{D}_w$ denotes the expected value of the power dissipated per unit area. The total wave energy E and the mean wave direction θ_{m} were given by

$$E=\int_0^{2\pi}e(\theta)d\theta \tag{6}$$

and

$$\theta_{\mathrm{m}}=\frac{1}{E}\int_0^{2\pi}\theta e(\theta)d\theta \tag{7}$$

The resolution of directional spreading of waves was set to 10° in this study, and the lower and upper directional limits were defined as −90° and 90°, respectively. The root-mean-square wave height was calculated based on

$$H_{\mathrm{rms}}=\sqrt{\frac{8\overline{E}}{\rho g}} \tag{8}$$

For monochromatic waves over an alongshore uniform beach, the wave energy balance equation becomes

$$\frac{\partial Ec_{gx}}{\partial x}+\overline{D}_w=0 \tag{9}$$

The wave direction variation over the beach was determined by the Snell's law. The wave height was calculated as Eqn (8). The linear dispersion relation relates the wave number of a wave to its frequency as

$$\omega^2-gk\tanh(kh)=0 \tag{10}$$

The nonlinear dispersion relation proposed by Kirby and Dalrymple (1986) was employed to examine the effects of amplitude dispersion on depth inversion and wave predictions as

$$\omega^2=gk\left(1+\mathscr{F}_1(kh)\varepsilon^2D\right)\tanh\left(kh+\mathscr{F}_2(kh)\varepsilon\right) \tag{11}$$

$$D=\frac{\cosh(4kh)+8-2\tanh^2(kh)}{8\sinh^4(kh)} \tag{12}$$

$$\mathscr{F}_1(kh)=\tanh^5(kh) \tag{13}$$

$$\mathscr{F}_2(kh)=\left[\frac{kh}{\sinh(kh)}\right]^4 \tag{14}$$

where $\varepsilon=k|A|$ and $|A|=1/2H$ (Catálan and Haller, 2008). The group velocity c_g was computed by

$$c_g=\frac{\partial\omega}{\partial k} \tag{15}$$

2.2. Physics-informed neural networks

To solve the depth inversion problems over an alongshore varying barred beach and circular shoal with linear dispersion relation, the corresponding residuals were defined as

$$f_1(x,y,\theta):=\frac{\partial ec_{gx}}{\partial x}+\frac{\partial ec_{gy}}{\partial y}+\frac{\partial ec_{g\theta}}{\partial\theta}+d_w \tag{16}$$

$$f_2(x,y):=\omega^2-gk\tanh(kh) \tag{17}$$

To consider the effects of amplitude dispersion on depth inversion and wave field reconstruction for nonlinear waves over the alongshore uniform beach, the residuals were determined as

$$f_1(x):=\frac{\partial Ec_{gx}}{\partial x}+\overline{D}_w \tag{18}$$

$$f_2(x):=\omega^2-gk\left(1+\mathscr{F}_1(kh)\varepsilon^2D\right)\tanh\left(kh+\mathscr{F}_2(kh)\varepsilon\right) \tag{19}$$

These residuals were used as restraints during the training of PINNs to generate physically consistent predictions. Additionally, the wave measurements scattered in the computational domain were also used to constrain the model, such as wave height and wave number.

The schematic representation of the algorithm for simultaneous mapping of nearshore bathymetry (depth inversion) and wave field using Method A is shown in Fig. 1. Because e is related to (x,y,θ) while k and d only depend on (x,y), composite neural networks (i.e., $\mathscr{N}_1$ and $\mathscr{N}_2$) were utilized to estimate water depth and simulate nearshore wave fields in this study. The loss function consists of two main parts. The first part corresponds to the collocation points (i.e., residual loss), where the physical constraints were imposed to encourage Eqns (16) and (17) (or Eqns (18) and (19)) to equal zero. In general, the collocation points could be grid points or random points inside the computational domain (Lu et al., 2021), and the former one was applied in this study.

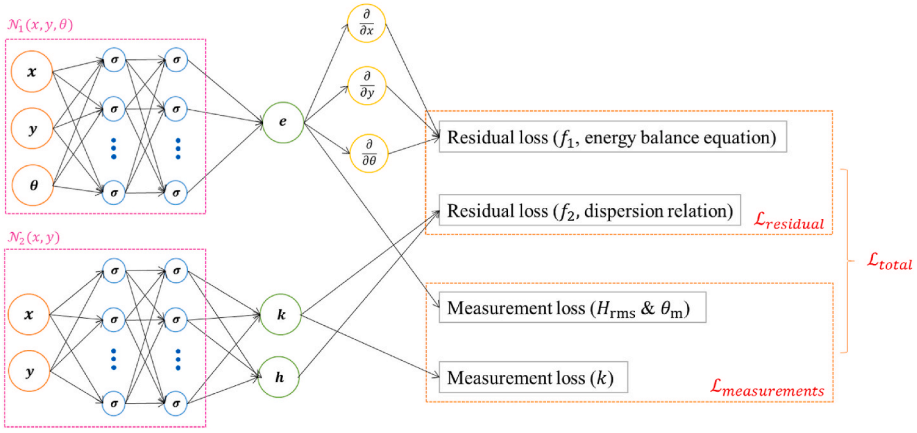

Fig. 1. A schematic representation of Method A for solving the depth inversion problems. $\mathcal{N}_1$ and $\mathcal{N}_2$ are the networks for simulating e as well as k and h, respectively. σ represents the node in each layer. $\frac{\partial}{\partial x}$, $\frac{\partial}{\partial y}$, and $\frac{\partial}{\partial \theta}$ are the partial derivative relative to x, y, and θ, respectively.

Automatic differentiation was used to calculate the partial derivatives in the residual expression (Kissas et al., 2020). The second part encouraged the outputs of PINNs to match wave parameters obtained from field observations (i.e., measurement loss). Therefore, the total loss function for solving the depth inversion problem of linear waves is given as

$$\mathscr{L}_{total} = \mathscr{L}_{residual} + \mathscr{L}_{measurements} = \mathscr{L}_{f_1} + \lambda_{f_2} \times \mathscr{L}_{f_2} + \lambda_{H_{rms}} \times \mathscr{L}_{H_{rms}} + \lambda_{\theta_m} \times \mathscr{L}_{\theta_m} + \lambda_k \times \mathscr{L}_k \quad (20)$$

where $\lambda_{f_2}, \lambda_{H_{rms}}, \lambda_{\theta_m}$, and λ_k are the weighting coefficients determined by the learning rate annealing algorithm for balancing the interplay between different terms in the loss function (Jin et al., 2021). The learning rate annealing algorithm can improve the simulation accuracy by using gradient statistics to determine proper weights adaptively to each term in loss functions (e.g., Wang et al., 2022a). In this study, the mean squared error (*MSE*) was employed to represent the loss functions and is given for each term by

$$\mathscr{L}_{f_1} = \frac{1}{N_f} \sum_{i=1}^{N_f} \left(f_1^i \left(x_f^i, y_f^i, \theta_f^i \right) \right)^2 \quad (21)$$

$$\mathscr{L}_{f_2} = \frac{1}{N_f} \sum_{i=1}^{N_f} \left(f_2^i \left(x_f^i, y_f^i \right) \right)^2 \quad (22)$$

$$\mathscr{L}_{H_{rms}} = \frac{1}{N_{H_{rms}}} \sum_{i=1}^{N_{H_{rms}}} \left({H_{rms}}^i \left(x_{H_{rms}}^i, y_{H_{rms}}^i \right) - {H_{rms}^*}^i \right)^2 \quad (23)$$

$$\mathscr{L}_{\theta_m} = \frac{1}{N_{\theta_m}} \sum_{i=1}^{N_{\theta_m}} \left({\theta_m}^i \left(x_{\theta_m}^i, y_{\theta_m}^i \right) - {\theta_m^*}^i \right)^2 \quad (24)$$

$$\mathscr{L}_k = \frac{1}{N_k} \sum_{i=1}^{N_k} \left(k^i \left(x_k^i, y_k^i \right) - k^{*i} \right)^2 \quad (25)$$

where $\{{H_{rms}}^i(x_{H_{rms}}^i, y_{H_{rms}}^i)\}_{i=1}^{N_{H_{rms}}}$, $\{{\theta_m}^i(x_{\theta_m}^i, y_{\theta_m}^i)\}_{i=1}^{N_{\theta_m}}$, and $\{k^i(x_k^i, y_k^i)\}_{i=1}^{N_k}$ denote the PINN outputs of H_{rms}, θ_m, and k, respectively. H_{rms}^*, θ_m^*, and k^* are the targets (labels) of H_{rms}, θ_m, and k, respectively. $\{(x_f^i, y_f^i, \theta_f^i)\}_{i=1}^{N_{H_{rms}}}$ represents collocation points that are uniformly placed inside the computational domain to minimize the loss of residuals.

Regarding Method B for estimating bathymetry and wave fields, we used the same algorithm and loss functions as the ones in Wang et al. (2022a). Notice that we assumed wave numbers and wave angles were unknown in Method B, so they were not applied as the training data for the model, which is a slight difference compared to the algorithm in Wang et al. (2022a). In this study, we used hyperbolic tangent as the activation function, and the deep neural nets were initialized with Xavier initialization (Glorot and Bengio, 2010). The network structure was kept identical to four hidden layers of 30 nodes for each test case. More details on the selected optimizer, learning rates, and settings of the measurements and collocation points shall be given in Sections 2.2.1 to 2.2.3. The training was implemented on an NVIDIA v100-sxm2 GPU with the TensorFlow platform. The training of the PINN models took about 3–6 h for different test cases.

2.2.1. *Alongshore varying barred beach*

The wave condition offshore of the alongshore varying barred beach was set as $H_{rms} = 1$ m and peak wave period (T_p) = 8 s. The peak wave period remains constant over the entire computational domain. The incident wave angle follows the directional distribution of $\cos^m(\theta - \theta_m)$ with $\theta_m = -30^\circ$ and m = 20. Fig. 2 shows the bathymetry of the alongshore varying barred beach and the XBeach-simulated H_{rms}. The computational domain extended from $x = 0$ to 980 m in the cross-shore direction and from $y = 20$ to 480 m in the alongshore direction with a resolution of 10 m. The resolution of directional spreading of waves ($d\theta$) was set to 10° in both XBeach and PINN models, and the lower and upper directional limits were defined as −90°–90°, respectively. A total of 4 653 collocation points were uniformly distributed from x = 0-980 m and y = 20-480 m to constrain learning for generating physically consistent predictions.

The test case of this alongshore varying barred beach was applied to examine the performance of Method A and Method B for simultaneous mapping of the bathymetry and wave fields. For Method A, it was assumed that the wave number and wave angle were known at every location, meaning that the wave number and wave angle over the entire study area were used as training data for the model. We randomly selected a total of 100 training points of H_{rms} over the entire domain. Fifteen of them are in the offshore area. Thirty-five are in the shoaling zone. The rest of the 50 points are in the surf zone. Twenty validation points were selected randomly from the rest of the dataset, and the remaining data were utilized as testing points. The total number of training points is about 2% of the entire computational data. To get better accuracy, more training points were placed in the shoaling and breaking zones since strong wave height variations happen in these two areas. In reality, we may not know where the shoaling and breaking zones are because the bathymetry and offshore wave conditions are unknown. It was assumed that the surf zone is from 800 m to 980 m, and more training points were placed in this region. The sensitivity of the performance of PINNs to the training points of H_{rms} is further discussed in Section 4.1.

In field experiments, nearshore bathymetric data can be collected across multiple cross-shore transects spaced about 50 m apart (e.g., US

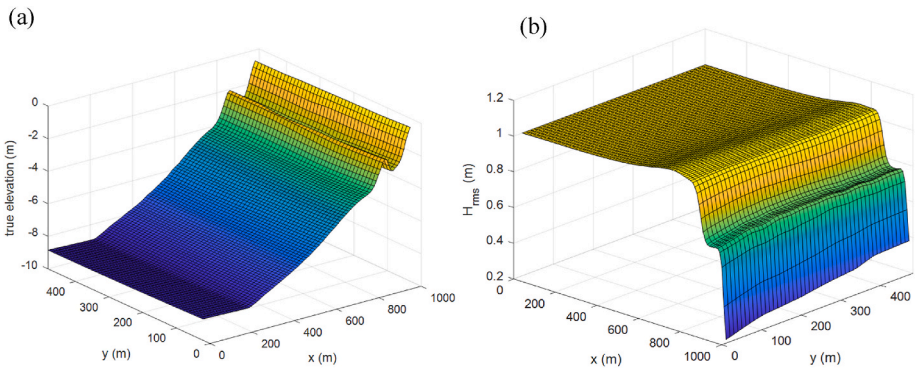

Fig. 2. (a) The bathymetry of the alongshore varying barred beach and (b) the XBeach-simulated wave height.

Army Engineering and Research Center Field Research Facility (FRF) in Duck, NC). Normally, these surveys are then interpolated linearly in the cross-shore and alongshore directions to obtain the bathymetry of the entire space of interest, which is then used as an input to physics-based numerical models (e.g., Chen et al., 2003) to simulate the nearshore wave processes. To estimate the bathymetry and reconstruct wave fields with Method B, we used some measured data of water depth along the cross-shore transects and wave heights scattered between adjacent transects as training points. The resolution of measured bathymetric data in the alongshore and cross-shore directions was set as 50 m (or 110 m) and 10 m, respectively. The measured wave height locations were randomly selected inside the domain with more data placed nearshore as training data (i.e., x = 800–980 m). Twenty validation points of H_{rms} and d were selected randomly from the rest of the dataset, and the remaining data were utilized as testing points. The PINN-predicted wave height and water depth were then compared to the true data to examine the performance of Method B. In this case, the synthetic data from XBeach were used as the "observational data" for demonstration purposes. Testing of the inverse PINN models against real field observations will be carried out in future studies.

For both mapping methods, Adam (adaptive moment estimation) and L-BFGS-B (*limited memory Broyden–Fletcher–Goldfarb–Shanno with boundaries)* were used as network training functions (e.g., Kingma and Ba, 2014; Liu and Nocedal, 1989). The Adam optimizer was employed to produce a better set of initial neural network variables, and L-BFGS-B was used to further fine-tune the PINN networks to minimize test errors (Jin et al., 2021). The initial learning rate of Adam was set to 10^{-4} and then decreased to 80% of the previous rate every 5 000 iterations. 8×10^4 Adam iterations were implemented before the L-BFGS-B training, which was then automatically terminated based on the increment tolerance. The error statistics were computed to quantify the prediction skills of PINNs, including root mean square error (*RMSE*) and correlation coefficient square (R^2).

2.2.2. Circular shoal

The simulation accuracy of Method B for solving depth inversion problems was also examined using experimental laboratory data. A series of physical experiments on wave propagation over a circular shoal were carried out by Chawla et al. (1996) in a directional wave basin. In this study, test case 4 of the laboratory experiment was utilized as the testbed to examine the performance of the inverse PINN model. A total of 126 locations in the wave basin were set to record the wave heights in the cross-shore and alongshore directions during the laboratory experiments. Here, we used 50% of the 126 H_{rms} measurements as training data together with the corresponding water depth to reconstruct the entire wave field and estimate the bathymetry. The water depths offshore and at two lateral boundaries were also applied as the training data. Ten validation points of H_{rms} and d were selected randomly from the rest of the dataset, and the remaining data were utilized as testing points of H_{rms}. It is worth mentioning that the same dataset of test case 4 was also utilized as one of the testbeds in Wang et al. (2022a), which developed the *NWnets* to reconstruct entire wave fields assuming the water depth data were known everywhere. Notice that although the training data also included limited water depth measurements in Method B, this study aims to simultaneously estimate the bathymetry of the entire domain and reconstruct the wave field, which is a significant difference from the work by Wang et al. (2022a). The computational domain, collocation points, and network structures in Method B were kept the same as the ones used in Wang et al. (2022a).

2.2.3. Alongshore uniform barred beach

PINN models offer an opportunity to account for the impact of wave amplitude dispersion on depth inversion in nonlinear wave systems, because wave heights and bathymetry can be simultaneously estimated by PINNs. To test the PINNs' ability to account for the effect of wave nonlinearity in the nearshore, we used the nonlinear dispersion relation instead of the linear dispersion relation to reconstruct the wave field and estimate the bathymetry over an alongshore uniform barred beach with known wave numbers. The nonlinear dispersion relation proposed by Kirby and Dalrymple (1986) was employed in this study, as shown by Eqn (11). The training data of wave height and wave number for developing PINNs were generated using iterative solutions in this case. Numerical solutions to Eqns (9) and (11) to (15) were used as a reference for comparison of PINN results with different dispersion relations.

The cross-shore distance from the offshore location was set as x, and the entire computational domain extended from $x = 0$ to 1000 m. The wave boundary condition of the nonlinear waves was set as $H = 1$ m, $T = 8$ s, and the incident wave angle of 30°. The Ursell number ($Ur = HL^2/h^3$) ranged from 300 to 600 over the domain. The wave height training data was set at x = 100 m, and wave numbers were known every 4 m from x = 0–1 000 m. Twenty validation points were selected randomly from the rest of the dataset, and the remaining data were utilized as testing points. Similar to the PINN model for estimating the water depth of an alongshore varying barred beach, Adam and L-BFGS-B were used as network training functions, with 4×10^4 Adam iterations conducted before L-BFGS-B started. To examine the prediction performance of the model for reconstructing the wave field, the outputs of H were compared to the numerical solutions to the wave energy balance equation with either the linear or nonlinear dispersion relation.

3. Results

3.1. Simultaneous mapping of bathymetry and wave field based on wave numbers and scarce measurements of wave height (Method A)

3.1.1. Water waves over an alongshore varying barred beach

In this section, the outputs from XBeach and PINNs were compared to determine the feasibility of using PINNs to estimate water depth and reconstruct wave fields over an alongshore varying barred beach with Method A. The comparison between the PINNs and XBeach outputs is

shown in Fig. 3. The contour plot in Fig. 3 (a) depicts the simulation error of PINN-simulated water depth with the black dots showing the locations of H_{rms} training points. It can be observed that PINNs have good prediction skills for estimating water depths with small errors (maximum error = 1.6%). The 3D plot in Fig. 3 (b) presents the PINN-simulated H_{rms}, which is in good agreement with the numerical results from XBeach. Also, the simulation outputs from the PINNs and XBeach are compared in Fig. 3 (c), showing that the PINN-predicted H_{rms} and θ_m correlated well with those from XBeach. Overall, the developed PINN model has a promising ability to simultaneously estimate water depths and reconstruct wave fields over an alongshore varying barred beach with known wave numbers and scarce wave heights (synthetic data from XBeach) applied as the training data.

3.1.2. Effects of amplitude dispersion on depth inversion and wave height prediction

To test the PINNs' ability to account for the effect of wave nonlinearity in the nearshore, we used the nonlinear dispersion relation instead of the linear dispersion relation to reconstruct the wave field and estimate the bathymetry over an alongshore uniform barred beach with known wave numbers (Method A). Fig. 4 (a) shows that the PINN outputs correlate well with the numerical solutions to Eqns (9)-(14) with the nonlinear dispersion relation embedded in the model. Such synthetic data are called "reference data" as mentioned in Section 2.2.3. We also estimated the nonlinear wave fields using PINNs with linear dispersion relation. It can be observed that the simulation skills of the PINN model embedded with the linear dispersion relation deteriorate in the surf zone (Fig. 4 (b)), suggesting that the linear PINN model has a similar pattern as cBathy in the nearshore. In other words, the PINN model embedded with the linear dispersion relation is not capable of learning the effect of nonlinear waves on the dispersion relation. This finding indicates that selecting an appropriate physical constraint is crucial for solving the depth inverse problems and reconstructing wave fields with sufficient accuracy. For field applications where the observed wave number vectors are strongly influenced by wave nonlinearity, it is expected that the nonlinear PINN model will produce more accurate water depth in the surf zone than existing methods.

3.2. Simultaneous mapping of bathymetry and wave field based on scarce measurements of wave height and water depth (Method B)

3.2.1. Water waves over a circular shoal

In this section, the simulation skill of Method B for estimating water depth and wave field was examined using the laboratory experimental data. Fig. 5 presents the outputs of wave heights and water depths from the inverse PINN model. Fig. 5 (c) shows good agreement between the experimental and PINN-simulated wave heights, as the PINN model captured the focusing of wave energy along the transects of *E-E* and *F–F* and the defocusing of wave energy along the transects of *C–C* and *D-D* (Fig. 5 (a)). Furthermore, water depths were well predicted at most of the locations by the PINN model. Fig. 5 (b) shows the spatial distribution of the depth inversion errors. It is seen that the majority of the PINN-inferred water depths have less than 4% error, while larger errors of depth estimation occur around the edge of the circular shoal. This can be explained by the fact that the water depths change dramatically near the edge of the shoal as the local gradients of the bathymetry are not continuous at the circular edge. We found that increasing the number of collocation points can improve the simulation accuracy (Table 1). However, the training time also increased dramatically when more collocation points were utilized. Thus, practical applications of PINNs need to balance the computational costs and the simulation accuracy when selecting the resolution of the collocation points.

3.2.2. Water waves over an alongshore varying barred beach

In this section, we examined the performance of Method B by estimating the water depth based on measured bathymetry along cross-shore transects and wave heights scattered between adjacent transects, an analog to the long-term nearshore surveys at FRF in Duck, NC. Fig. 6 shows the spatial distributions of the simulation errors in the PINN-predicted water depths and wave heights. The results indicate that

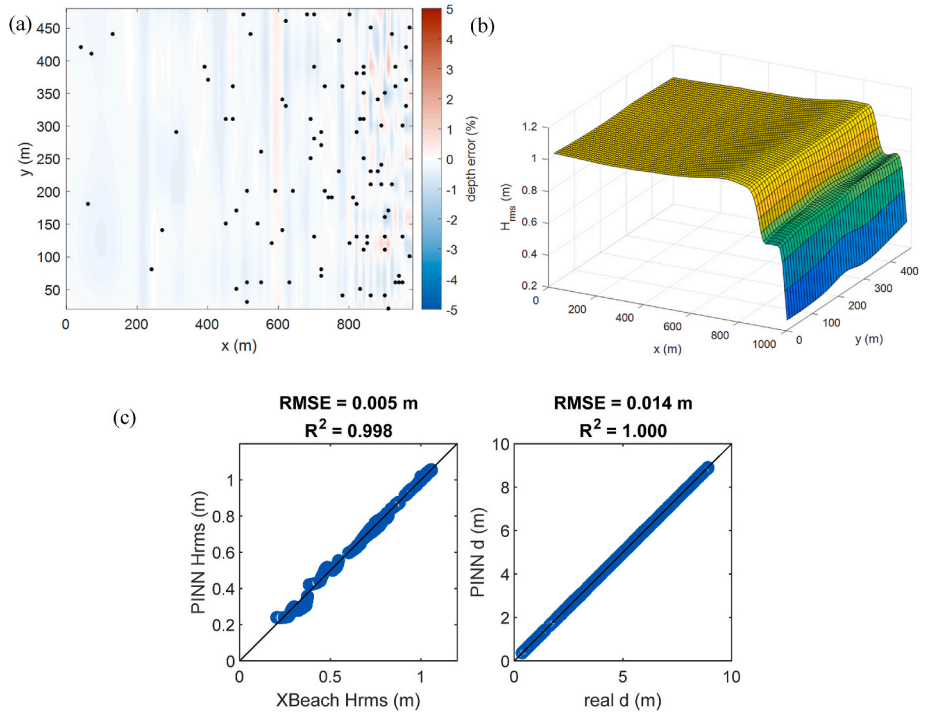

Fig. 3. Comparison between the XBeach and PINN outputs over the alongshore varying barred beach. (a) The simulation errors of the PINN-predicted depth. The black dots represent the locations of wave height training points; (b) spatial variation of the PINN-predicted wave heights; (c) scatter plots of the predicted H_{rms} and d (the plots only contain testing data).

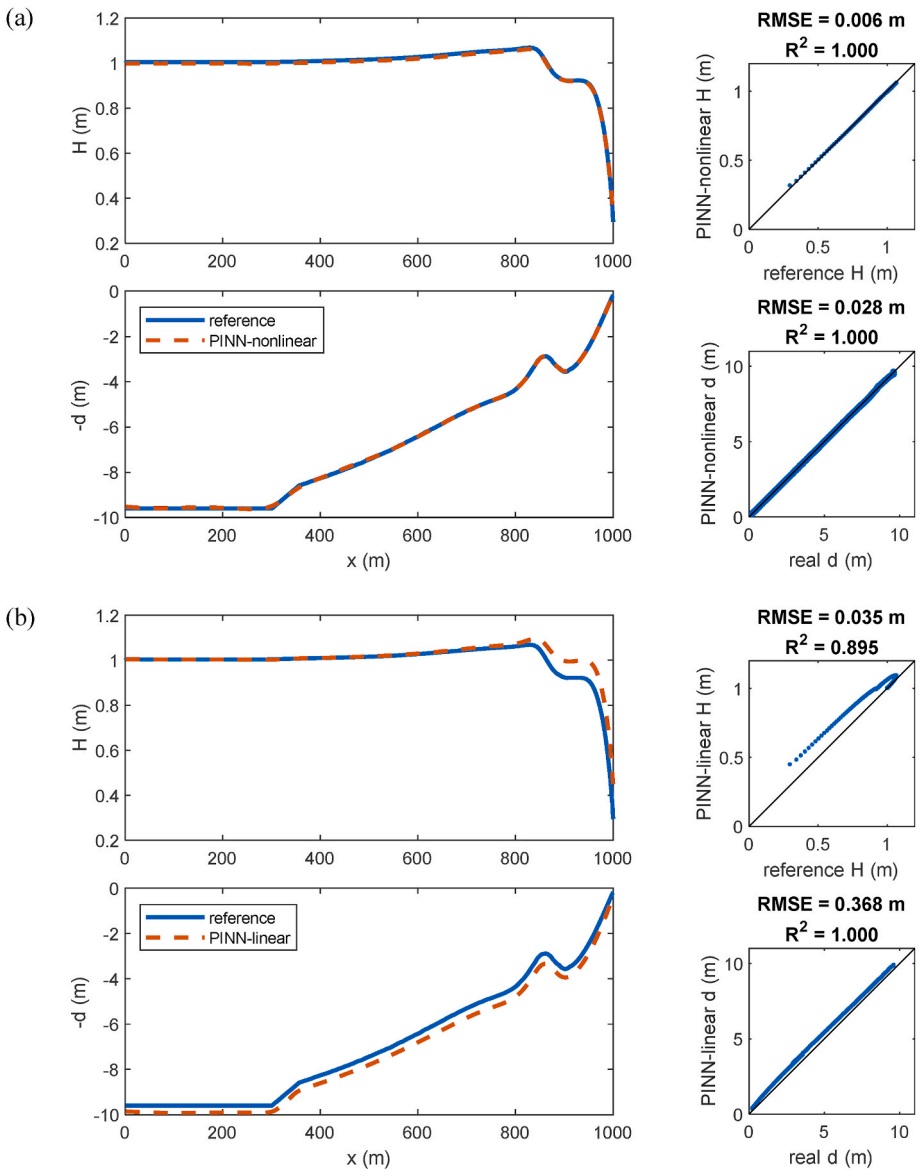

Fig. 4. Comparisons between reference and PINN-simulated H and water depth with (a) nonlinear dispersion relation and (b) linear dispersion relation. The scatter plots only contain testing data.

bathymetry and wave height can be well estimated by the developed PINN models with measured water depths along a limited number of cross-shore transects and scarce wave height measurements applied as training data (without wave number information). Compared to linear interpolation, the inverse PINN models provide a more accurate way to determine the water depths over the entire domain, because small-scale bathymetry changes between the cross-shore transects can be identified with the measured wave parameters.

4. Discussion

4.1. Strategies for improving simulation accuracy and efficiency in PINNs

The sensitivity of the model accuracy of PINNs to the number and distribution of training points of H_{rms} over the alongshore varying barred beach (Method A) is investigated in this section as an example. Because strong variations of wave height happen in the shoaling zone and surf zone, we used different numbers of training points of H_{rms} at x = 500–980 m. Table 2 shows the error statistics of PINN outputs when the training data of H_{rms} were at different locations. Unsurprisingly, the results indicate that the simulation accuracy of H_{rms} tended to increase when the number of training points increased, especially when more training points were placed close to the shore from x = 800–980 m. Also, it was found that maximum errors for both PINN-simulated H_{rms} and d happen nearshore (x = 800–980 m). This is because the wave height variation is higher due to the depth-limited wave breaking inside the surf zone. Therefore, to obtain a higher accuracy of wave height prediction, more training points should be placed nearshore. Since the wave number was assumed to be known at every point inside the computational domain, the accuracy of the estimated bathymetry is very good if amplitude dispersion is embedded in the PINN model. It is worth mentioning that the model does not require the wave number at every location as training points, and PINNs can still generate satisfactory results for solving the depth inverse problems (Section 3.1.2). In future studies, the model framework can be tested in the field where in-situ measurements and remote sensing data (e.g., LiDAR and stereo-video) are available (e.g., Wilson et al., 2014).

Similar to numerical simulations using conventional physics-based models, we need to retrain the model when the offshore wave conditions or the depth profiles change. However, transfer learning can be

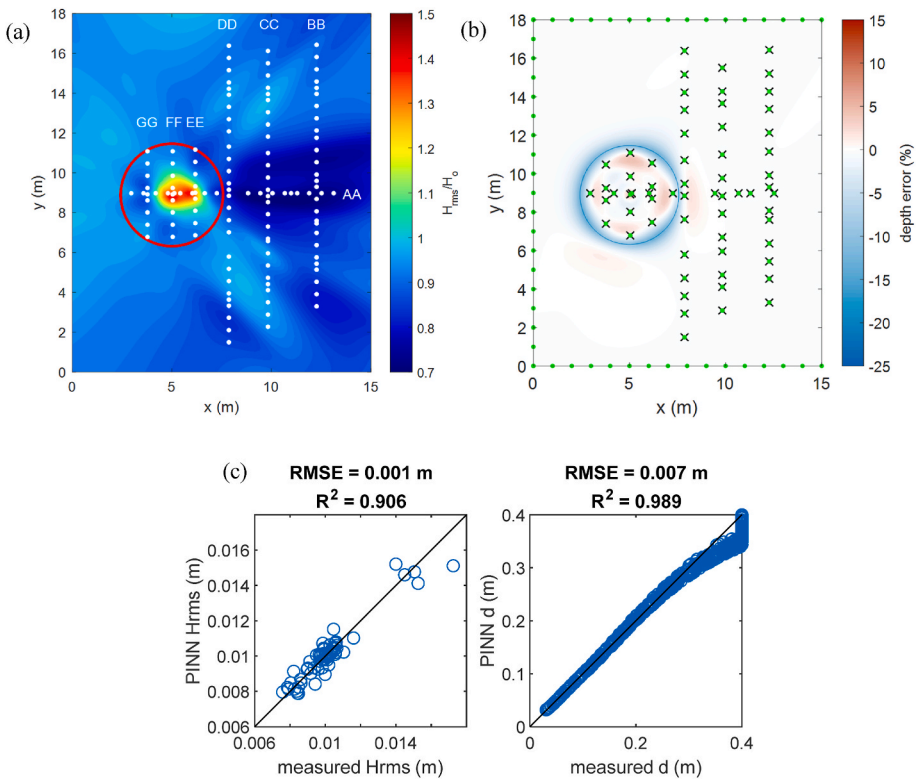

Fig. 5. (a) Spatial distribution of PINN-simulated wave heights. The white dots represent the locations of the entire 126 wave height measurements; (b) spatial distribution of the relative errors of PINN-simulated water depth. The error was divided by the local depth. The green dots and black crosses show the locations of water depth and wave height measurements as training data, respectively; (c) scatter plots of PINN-simulated and measured data of H_{rms} and d (the plots only contain testing data).

Table 1
Test errors of the PINN-simulated H_{rms} and d on the circular shoal with different resolutions of collocation points.

Resolution of collocation points (m)	*RMSE*		R^2		Computational time (hours)
	H_{rms} (m)	d (m)	H_{rms}	d	
0.2	0.001	0.007	0.906	0.986	5.9
0.4	0.001	0.008	0.902	0.980	3.5
0.8	0.001	0.014	0.887	0.947	2.8

used to accelerate the training of PINNs for simultaneous mapping waves and bathymetry when the following simulation has slightly different wave boundary conditions or depth profiles. Specifically, the pretrained PINNs can be applied to initialize the subsequent simulations other than training a new network from scratch (i.e., initialize the new network weights and bias using the parameters of the pretrained PINNs) (Jin et al., 2021). For instance, the PINNs for estimating bathymetry and wave fields over the alongshore varying barred beach with the boundary condition of $H_{rms} = 1$ m and $T_p = 8$ s have been well developed. Later, we would like to develop a second PINNs for estimating the water depths and wave fields over slightly different bathymetry and different offshore wave boundary conditions (e.g., $H_{rms} = 1.1$ m and $T_p = 7.8$ s). To accelerate the training of the new PINNs, we can initialize the second network weights and bias using the parameters of the pretrained PINNs with the boundary condition of $H_{rms} = 1$ m and $T_p = 8$ s, so that the computational efficiency can be improved. Future testing of transfer learning under realistic field conditions is needed.

4.2. Comparison with conventional ANN

The conventional ANN model is composed of densely interconnected information-processing nodes organized into layers (James et al., 2018; Wang et al., 2022b, 2022c). The main difference between ANN and PINNs is that the loss function of ANN only contains measurement loss, while PINNs contain measurement loss and residual loss (i.e., physics-informed). To examine the effect of physical regularization on the PINN results, we generated a simulation experiment using the conventional ANN model for estimating bathymetry and wave fields over the circular shoal with Method B as an example (Fig. 7). The ANN model setup and hyperparameter selection (e.g., activation function and learning rate) were kept the same as the ones used in the PINNs, except that the total loss function only contained the measurement loss without the residual loss (i.e., the ANN model was developed from scratch). The results show that the ANN-predicted wave height distribution has considerable errors, and the simulation errors of bathymetry increase significantly. The R^2 values for the ANN-predicted H_{rms} and d decreased to 0.56 and 0.95, respectively, and the *RMSE* value of d increased to 0.014 m. This pattern is more obvious in the domain where fewer training data were placed (e.g., domain to the left of transect of *D-D*), indicating that embedding the physics into the neural networks indeed improves the ML-model performance for solving depth inversion problems and reconstructing wave fields.

5. Conclusions

An accurate estimation of the nearshore bathymetry is critical for designing and operating many coastal projects because of the increasing coastal utilization and sea level rise. Usually, in-situ bathymetric surveys require specialized equipment and can be expensive and time-consuming to obtain. Thus, it is highly desirable to estimate the nearshore bathymetry using remote sensing techniques, which can cover a broader spatial and temporal range than the traditional in-situ instruments. In this study, we developed inverse PINN models to estimate nearshore bathymetry based on remote sensing data (i.e., wave number and significant wave height) by combining the prior knowledge of wave mechanics into the fully-connected neural networks.

Although the digital image processing of remote sensing data is not covered in this study, we can still investigate the feasibility of using remote sensing data to solve the depth inversion problem by training

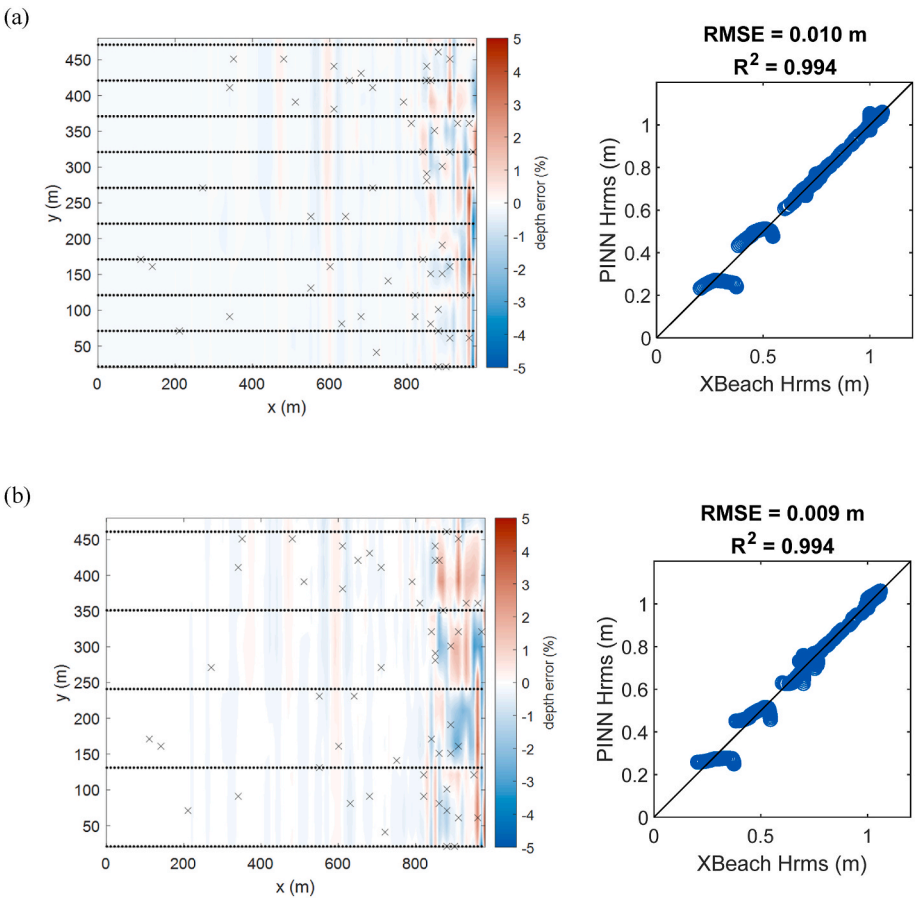

Fig. 6. Simulation errors of the PINN-predicted water depths and wave heights with (a) 10 cross-shore transects of 50m apart and (b) 5 cross-shore transects of 110 m apart. The black dots and crosses represent the locations of the training points for water depth and wave height, respectively. The scatter plots only contain testing data.

Table 2
Error statistics of the simulated H_{rms} and d over the alongshore varying barred beach using different training points of H_{rms} applied in Method A.

	RMSE		R^2		Max error	
	H_{rms} (m)	d (cm)	H_{rms}	d	H_{rms} (m)	d (cm)
o15n35o50[a]	0.005	1.450	0.998	1.000	0.171	1.63
o15n35o40	0.006	1.460	0.998	1.000	0.155	1.59
o15n35o30	0.017	1.520	0.984	1.000	0.409	1.72
o15n35o20	0.016	1.470	0.989	1.000	0.474	2.02
o15n35o10	0.032	1.460	0.979	1.000	0.452	2.24
o15n30o50	0.008	1.450	0.997	1.000	0.369	1.91
o15n20o50	0.008	1.450	0.996	1.000	0.350	1.91
o15n10o50	0.010	1.470	0.995	1.000	0.388	1.93

[a] o15n35o50 means 15, 35, and 50 training points of H_{rms} were set at x = 0–500 m, 500–800 m, and 800–980 m, respectively.

PINN models with the post-processed geophysical parameters. This study developed two methods to solve the depth inversion problems and estimate wave fields. Assuming surface wave number and limited wave height measurements are available from various remote sensing platforms or synthetic data from a physics-based model, the first method employed wave numbers and scarce measurements of wave height as training data. The second method applied scarce wave height and limited water depth measurements as training points to reconstruct bathymetry and wave fields. The results show that both methods are capable of simultaneously mapping the bathymetry and wave fields when the locations of scarce training points are appropriately distributed. Furthermore, the sensitivity of the PINN performance to the number and locations of training points of H_{rms} was investigated using water waves over an alongshore varying barred beach as an example. It was found that the *RMSE* of H_{rms} decreases when the number of training points increases. Moreover, if the total number of training points is fixed, higher accuracy can be obtained when more training points are placed in the surf zone.

One advantage of applying PINNs to solve bathymetry inversion problems is that wave height and bathymetry can be simultaneously estimated by PINN models. Thus, the effect of wave amplitude dispersion on depth inversion in nonlinear wave systems can be quantified directly without measuring the entire wave height field. In this study, we used the nonlinear dispersion relation instead of the linear dispersion relation together with the energy balance equation as the physical laws to reconstruct the wave field and estimate the bathymetry over an alongshore uniform barred beach with known wave numbers. The results show that the PINN outputs correlate well with the numerical solutions to the energy balance equation with the embedded amplitude dispersion. Additionally, it was found that PINNs cannot learn nonlinear wave characteristics with linear dispersion relation used as the constraint during the training process, which indicates that selecting an appropriate physical constraint is crucial for solving the depth inverse problems and reconstructing wave fields with sufficient accuracy.

This study is the first attempt to investigate the capability of PINNs for simultaneously mapping nearshore bathymetry and reconstructing wave fields with limited field data. Though the current results are encouraging, more studies are needed to further test the performance of PINNs under field conditions. In particular, it is important to quantify the potential errors of PINNs when remotely sensed data are inaccurate

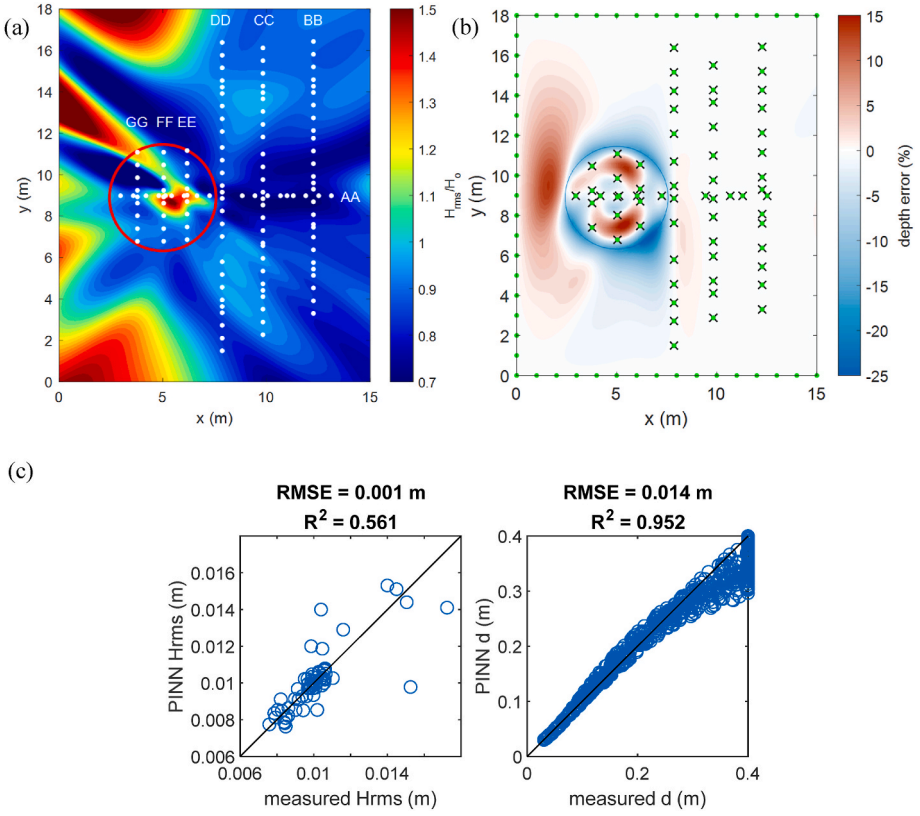

Fig. 7. (a) Spatial distribution of ANN-simulated wave height. The white dots represent the locations of the entire 126 wave height measurements; (b) the percentage errors of simulated water depth. The green dots and black crosses show the locations of water depth and wave height measurements, respectively; (c) scatter plots of PINN-simulated and measured data of H_{rms} and d (the plots only contain testing data).

and the embedded physics is incomplete.

Author credit statement

Qin Chen: Conceptualization, Methodology, Validation, Writing, Supervision, Funding acquisition.

Nan Wang: Methodology, Software, Validation, Writing.

Zhao Chen: Investigation, Writing- Reviewing and Editing.

Declaration of competing interest

The authors declare that they have no known competing financial interests or personal relationships that could have appeared to influence the work reported in this paper.

Data availability

Data will be made available on request.

Acknowledgments

This paper is based upon work supported by the National Science Foundation under Award No. 2139882. Any opinions, findings and conclusions or recommendations expressed in this paper are those of the authors and do not necessarily reflect the views of the National Science Foundation. Any use of trade, firm, or product names is for descriptive purposes only and does not imply endorsement by the U.S. Government.

References

Aarninkhof, S.G.J., Ruessink, B.G., Roelvink, J.A., 2005. Nearshore subtidal bathymetry from time-exposure video images. J. Geophys. Res. Ocean. 110.

Birkemeier, W.A., Mason, C., 1984. The CRAB: a unique nearshore surveying vehicle. J. Survey Eng. 110, 1–7.

Birrien, F., Castelle, B., Marieu, V., Dubarbier, B., 2013. On a data-model assimilation method to inverse wave-dominated beach bathymetry using heterogeneous video-derived observations. Ocean Eng. 73, 126–138.

Blenkinsopp, C.E., Turner, I.L., Allis, M.J., Peirson, W.L., Garden, L.E., 2012. Application of LiDAR technology for measurement of time-varying free-surface profiles in a laboratory wave flume. Coast. Eng. 68, 1–5.

Catálan, P.A., Haller, M.C., 2008. Remote sensing of breaking wave phase speeds with application to non-linear depth inversions. Coast. Eng. 55, 93–111.

Chawla, A.K., Kirby, J.T., Delaware., U. of, Engineering., D. of C., Delaware., U. of, Research., C. for A.C., Delaware., U. of, Laboratory., O.E, 1996. Wave Transformation over a Submerged Shoal. University of Delaware, Dept. of Civil Engineering, Center for Applied Coastal Research, Newark, Del.

Chen, Q., Dalrymple, R.A., Kirby, J.T., Kennedy, A.B., Haller, M.C., 1999. Boussinesq modeling of a rip current system. J. Geophys. Res. Ocean. 104, 20617–20637.

Chen, Q., Kirby, J.T., Dalrymple, R.A., Shi, F., Thornton, E.B., 2003. Boussinesq modeling of longshore currents. J. Geophys. Res. Ocean. 108.

Collins, A.M., Brodie, K.L., Bak, A.S., Hesser, T.J., Farthing, M.W., Lee, J., Long, J.W., 2020. Bathymetric inversion and uncertainty estimation from synthetic surf-zone imagery with machine learning. Rem. Sens. 12, 3364.

Dawson, M.S., Olvera, J., Fung, A.K., Manry, M.T., 1992. Inversion of surface parameters using fast learning neural networks. In: IGARSS '92 Int. Geosci. Remote Sens. Symp., pp. 910–912. https://doi.org/10.1109/IGARSS.1992.578294.

Dhamo, H., Tateno, K., Laina, I., Navab, N., Tombari, F., 2019. Peeking behind objects: layered depth prediction from a single image. Pattern Recogn. Lett. 125, 333–340.

Dugan, J.P., Morris, W.D., Vierra, K.C., Piotrowski, C.C., Farruggia, G.J., Campion, D.C., 2001. Jetski-based nearshore bathymetric and current survey system. J. Coast Res. 900–908.

Dugan, J.P., Suzukawa, H.H., Forsyth, C.P., Farber, M.S., 1996. Ocean wave dispersion surface measured with airborne IR imaging system. IEEE Trans. Geosci. Rem. Sens. 34, 1282–1284.

Eldesokey, A., Felsberg, M., Khan, F.S., 2019. Confidence propagation through cnns for guided sparse depth regression. IEEE Trans. Pattern Anal. Mach. Intell. 42, 2423–2436.

Gallego, G., Yezzi, A., Fedele, F., Benetazzo, A., 2011. A variational stereo method for the three-dimensional reconstruction of ocean waves. IEEE Trans. Geosci. Rem. Sens. 49, 4445–4457.

Ge, H., Liu, H., Zhang, L., 2020. Accurate depth inversion method for coastal bathymetry: introduction of water wave high-order dispersion relation. J. Mar. Sci. Eng. 8, 153.

Glorot, X., Bengio, Y., 2010. Understanding the difficulty of training deep feedforward neural networks. In: Proceedings of the Thirteenth International Conference on Artificial Intelligence and Statistics, pp. 249–256.
Grilli, S.T., 1998. Depth inversion in shallow water based on nonlinear properties of shoaling periodic waves. Coast. Eng. 35, 185–209.
Haller, M.C., Honegger, D., Catalan, P.A., 2014. Rip current observations via marine radar. J. Waterw. Port, Coast. Ocean Eng. 140, 115–124.
Holman, R., Plant, N., Holland, T., 2013. cBathy: a robust algorithm for estimating nearshore bathymetry. J. Geophys. Res. Ocean. 118, 2595–2609.
Honegger, D.A., Haller, M.C., Holman, R.A., 2019. High-resolution bathymetry estimates via X-band marine radar: 1. beaches. Coast. Eng. 149, 39–48.
James, S.C., Zhang, Y., O'Donncha, F., 2018. A machine learning framework to forecast wave conditions. Coast. Eng. 137 https://doi.org/10.1016/j.coastaleng.2018.03.004.
Janssen, T.T., Battjes, J.A., 2007. A note on wave energy dissipation over steep beaches. Coast. Eng. 54, 711–716.
Jin, X., Cai, S., Li, H., Karniadakis, G.E., 2021. NSFnets (Navier-Stokes flow nets): physics-informed neural networks for the incompressible Navier-Stokes equations. J. Comput. Phys. 426, 109951.
Kahana, A., Turkel, E., Dekel, S., Givoli, D., 2020. Obstacle segmentation based on the wave equation and deep learning. J. Comput. Phys. 413, 109458.
Kennedy, A.B., Dalrymple, R.A., Kirby, J.T., Chen, Q., 2000. Determination of inverse depths using direct Boussinesq modeling. J. Waterw. Port, Coast. Ocean Eng. 126, 206–214.
Kingma, D.P., Ba, J., 2014. Adam: A Method for Stochastic Optimization arXiv Prepr. arXiv1412.6980.
Kirby, J.T., Dalrymple, R.A., 1986. An approximate model for nonlinear dispersion in monochromatic wave propagation models. Coast. Eng. 9, 545–561.
Kissas, G., Yang, Y., Hwuang, E., Witschey, W.R., Detre, J.A., Perdikaris, P., 2020. Machine learning in cardiovascular flows modeling: predicting arterial blood pressure from non-invasive 4D flow MRI data using physics-informed neural networks. Comput. Methods Appl. Mech. Eng. 358, 112623.
Lewis, J.M., Lakshmivarahan, S., Dhall, S., 2006. Dynamic Data Assimilation: a Least Squares Approach. Cambridge University Press.
Liu, D.C., Nocedal, J., 1989. On the limited memory BFGS method for large scale optimization. Math. Program. 45, 503–528.
Lu, L., Meng, X., Mao, Z., Karniadakis, G.E., 2021. DeepXDE: a deep learning library for solving differential equations. SIAM Rev. 63, 208–228.
Lunz, S., Öktem, O., Schönlieb, C.-B., 2018. Adversarial Regularizers in Inverse Problems arXiv Prepr. arXiv1805.11572.
Martins, K., Bonneton, P., De Viron, O., Turner, I.L., Harley, M.D., Splinter, K., 2023. New perspectives for nonlinear depth-inversion of the nearshore using Boussinesq theory. Geophys. Res. Lett. 50, e2022GL100498.
Pilozzi, L., Farrelly, F.A., Marcucci, G., Conti, C., 2018. Machine learning inverse problem for topological photonics. Commun. Phys. 1, 1–7.
Raissi, M., Wang, Z., Triantafyllou, M.S., Karniadakis, G.E., 2019. Deep learning of vortex-induced vibrations. J. Fluid Mech. 861, 119–137.
Roelvink, D., Reniers, A., Van Dongeren, A.P., De Vries, J.V.T., McCall, R., Lescinski, J., 2009. Modelling storm impacts on beaches, dunes and barrier islands. Coast. Eng. 56, 1133–1152.
Ruggiero, P., Kaminsky, G.M., Gelfenbaum, G., Voigt, B., 2005. Seasonal to interannual morphodynamics along a high-energy dissipative littoral cell. J. Coast Res. 21, 553–578.
Salim, A., Wilson, G., 2021. Validation and analysis of a 1-D variational assimilation scheme for bathymetry inversion. Coast. Eng. 167, 103895.
Vamaraju, J., Sen, M.K., 2019. Unsupervised physics-based neural networks for seismic migration. Interpretation 7, SE189–SE200.
Van Dongeren, A., Plant, N., Cohen, A., Roelvink, D., Haller, M.C., Catalán, P., 2008. Beach Wizard: nearshore bathymetry estimation through assimilation of model computations and remote observations. Coast. Eng. 55, 1016–1027.
Wang, N., Chen, Q., Chen, Z., 2022a. Reconstruction of nearshore wave fields based on physics-informed neural networks. Coast. Eng., 104167
Wang, N., Chen, Q., Zhu, L., Sun, H., 2022b. Integration of data-driven and physics-based modeling of wind waves in a shallow estuary. Ocean Model., 101978 https://doi.org/10.1016/j.ocemod.2022.101978.
Wang, N., Chen, Q., Zhu, L., Wang, H., 2022c. Data-driven modeling of wind waves in upper Delaware Bay with living shorelines. Ocean Eng. 257, 111669 https://doi.org/10.1016/j.oceaneng.2022.111669.
Willard, J., Jia, X., Xu, S., Steinbach, M., Kumar, V., 2020. Integrating Physics-Based Modeling with Machine Learning: A Survey arXiv Prepr. arXiv2003.04919.
Wilson, G., Berezhnoy, S., 2018. Surfzone state estimation, with applications to quadcopter-based remote sensing data. J. Atmos. Ocean. Technol. 35, 1881–1896.
Wilson, G.W., Özkan-Haller, H.T., Holman, R.A., Haller, M.C., Honegger, D.A., Chickadel, C.C., 2014. Surf zone bathymetry and circulation predictions via data assimilation of remote sensing observations. J. Geophys. Res. Ocean. 119, 1993–2016.
Yoo, J., Fritz, H.M., Haas, K.A., Work, P.A., Barnes, C.F., 2011. Depth inversion in the surf zone with inclusion of wave nonlinearity using video-derived celerity. J. Waterw. Port, Coast. Ocean Eng. 137, 95–106.